

Trace elements in magnetite as petrogenetic indicators

Sarah A. S. Dare · Sarah-Jane Barnes · Georges Beaudoin ·
Julien Méric · Emilie Boutroy · Christophe Potvin-Doucet

Received: 12 February 2014 / Accepted: 18 May 2014 / Published online: 10 June 2014
© Springer-Verlag Berlin Heidelberg 2014

Abstract We have characterized the distribution of 25 trace elements in magnetite (Mg, Al, Si, P, Ca, Sc, Ti, V, Cr, Mn, Co, Ni, Cu, Zn, Ga, Ge, Y, Zr, Nb, Mo, Sn, Hf, Ta, W, and Pb), using laser ablation ICP-MS and electron microprobe, from a variety of magmatic and hydrothermal ore-forming environments and compared them with data from the literature. We propose a new multielement diagram, normalized to bulk continental crust, designed to emphasize the partitioning behavior of trace elements between magnetite, the melt/fluid, and co-crystallizing phases. The normalized pattern of magnetite reflects the composition of the melt/fluid, which in both magmatic and hydrothermal systems varies with temperature. Thus, it is possible to distinguish magnetite formed at different degrees of crystal fractionation in both silicate and sulfide melts. The crystallization of ilmenite or sulfide before magnetite is recorded as a marked depletion in Ti or Cu, respectively. The chemical signature of hydrothermal magnetite is distinct being depleted in elements that are relatively immobile during alteration and commonly enriched in elements that are highly incompatible into magnetite (e.g., Si and Ca). Magnetite formed from low-temperature fluids has the lowest overall abundance of trace elements due to their lower solubility. Chemical zonation of magnetite is rare but occurs in some hydrothermal deposits where laser mapping reveals oscillatory zoning, which records the changing conditions and

composition of the fluid during magnetite growth. This new way of plotting all 25 trace elements on 1 diagram, normalized to bulk continental crust and elements in order of compatibility into magnetite, provides a tool to help understand the processes that control partitioning of a full suit of trace elements in magnetite and aid discrimination of magnetite formed in different environments. It has applications in both petrogenetic and provenance studies, such as in the exploration of ore deposits and in sedimentology.

Keywords Magnetite · Trace elements · Mineral deposits · Magmatic · Hydrothermal · Petrogenesis

Introduction

Magnetite forms under a wide variety of conditions, crystallizing at high temperature from silicate and sulfide melts or precipitating at lower temperatures from hydrothermal fluids. Due to a large number of minor and trace element substitutions into magnetite, these different conditions lead to distinctive trace element signatures in magnetite. Recent analytical developments make it possible to determine a much wider range of trace elements than previously, and at lower concentrations (sub-ppm). Magnetite is a major component in the ferromagnetic fraction of heavy mineral separates from surficial sediments such as till. As such, there is growing interest in using the trace element signature of magnetite as provenance indicators, both in the exploration of ore deposits (Dupuis and Beaudoin 2011; Nadoll et al. 2014) and in sedimentology (Grigsby 1990; Razjigaeva and Naumova 1992; Yang et al. 2009). In order to use magnetite as a provenance indicator for mineral exploration, it is necessary to understand the processes that control the trace element concentrations in magnetite.

One of the major challenges is to establish which trace element variations in magnetite are significant and systematic.

Editorial handling: B. Lehmann

Electronic supplementary material The online version of this article (doi:10.1007/s00126-014-0529-0) contains supplementary material, which is available to authorized users.

S. A. S. Dare (✉) · S.-J. Barnes · J. Méric · C. Potvin-Doucet
Sciences de la Terre, Université du Québec à Chicoutimi (UQAC),
Saguenay, Québec, Canada G7H 2B1
e-mail: sasdare@hotmail.com

G. Beaudoin · E. Boutroy
Université Laval, Québec, Québec, Canada G1V 0A6

Modern laser ablation-ICP-MS (LA-ICP-MS) systems provide results for ~20–25 trace elements in magnetite with detection limits typically below the ppm level. In comparison, analysis of magnetite by electron microprobe can provide results for up to 12 elements in trace mode with detection limits at the level of 10 to 100 s of ppm (Dupuis and Beaudoin 2011). Some studies use a statistical approach, such as principal component analysis (e.g., Grigsby 1990; Nadoll et al. 2012), or an empirical approach based on a large database to identify combinations of elements and/or element ratios to determine discrimination diagrams (Dupuis and Beaudoin 2011; Nadoll et al. 2014). Others have concentrated on petrogenesis of individual deposit types (Reguir et al. 2008; Pecoits et al. 2009; Rusk et al. 2010; Dare et al. 2012; Angerer et al. 2013). This contribution considers trace elements in magnetite from well-characterized samples from different magmatic settings, which are then compared to examples of magnetite from a variety of hydrothermal settings, to establish which processes are important and which elements are the most diagnostic. All 25 trace elements (Mg, Al, Si, P, Ca, Sc, Ti, V, Cr, Mn, Co, Ni, Cu, Zn, Ga, Ge, Y, Zr, Nb, Mo, Sn, Hf, Ta, W, and Pb) are presented on a new multielement variation diagram, normalized to bulk continental crust and elements in order of compatibility into magnetite, that facilitates interpretation of the data in terms of processes and aids the characterization of magnetite from different settings. Our new multielement variation diagram has a wide breadth of applications from petrogenesis of magmatic rocks and ore deposits to provenance studies in mineral exploration and in sedimentology.

Samples and methodology

Magnetite-bearing samples from a wide range of environments (Table 1) were analyzed, and compared to data previously published, to illustrate the utility of the new multielement diagram. Magmatic magnetite that crystallized from high-temperature silicate melts, of intermediate composition, are from Fe-Ti-V-P deposits hosted in mafic-ultramafic-layered intrusions (Bushveld Complex, S. Africa and Sept Iles, Canada) and massif-type anorthosites (Lac St. Jean, Canada). Magnetite in massive sulfide from Ni-Cu-platinum-group-element (PGE) deposits (e.g., Sudbury and Voisey's Bay, Canada) represent magnetite formed from magmatic sulfide liquid (Dare et al. 2012; Boutroy et al. 2014). Magnetite from hydrothermal and sedimentary environments (see Table 1 for details), listed in order of decreasing temperature, include samples from iron-oxide-copper-gold (IOCG), porphyry-Cu, retrograde Fe-skarn, carbonate alteration in serpentinite, and banded iron formation (BIF) deposits. Many hydrothermal deposits, such as porphyry-Cu, IOCG, and skarn, typically form from fluids associated with subduction-related magmas of intermediate to felsic

composition, which commonly also form the host rock of some of these deposits. Magnetite in andesite (N. Chile) and I-type granite (Canada) were analyzed and compared to magnetite data compiled from the literature to demonstrate that they are representative of these rock types (Table 1). Due to the limited amount of LA-ICP-MS data available in the literature for the majority of trace elements, the compilation also includes electron microprobe data for the minor elements.

The LA-ICP-MS system used at LabMaTer, UQAC, is a Resonetics Resolution M-50 Excimer 193 nm laser coupled with an Agilent 7700x ICP-MS. The certified reference material GSE-1g was used for calibration and Fe, as determined by electron microprobe at Université Laval, used as the recovery element. Using a range of beam sizes from 33 to 75 μm , depending on grain size, lines were ablated across the grains in order to observe any zonation, in which case the zoned grain was mapped in detail using electron microprobe and LA-ICP-MS. During LA-ICP-MS, any fine-grained exsolution lamellae (e.g., ilmenite, spinel) present in magnetite were incorporated into the analysis and thus better represent the initial composition of the Fe-Ti oxide before subsolidus oxy-exsolution process occurred (Dare et al. 2012). Details of the analytical methods are given as supplemental information in the [Electronic Appendix](#).

Magnetite in magmatic systems

As a high-temperature melt cools, crystal fractionation changes the composition of the residual liquid according to the partitioning behavior of elements into the crystallizing phases. We can demonstrate that the composition of magnetite records the fractionation of not only silicate melts (Fig. 1) but also sulfide melts (Dare et al. 2012; Boutroy et al. 2014). The concentration of an element in magnetite depends on (a) the concentration of the element in the liquid from which it crystallizes, (b) whether other minerals crystallizing at the same time are competing for that element, and (c) partition coefficient (D) of the element into magnetite, which can vary up to several orders of magnitude with composition of the silicate melt, temperature, pressure, oxygen fugacity ($f\text{O}_2$), and cooling rate, see reviews in Mollo et al. (2013) and Nadoll et al. (2014).

We developed a multielement variation diagram (Fig. 1), taking into consideration the above factors that influence the concentration of trace elements into magnetite, in order to facilitate the interpretation of data, as follows. The 25 trace elements are plotted in order of increasing compatibility into magnetite, using the compilation of experimental and empirical partition coefficients between magnetite and silicate magmas of intermediate composition presented in Dare et al. (2012). The magnetite data is normalized to bulk

Table 1 Sample descriptions and trace element concentrations of magnetite analyzed by laser ablation-ICP-MS compared to some previously published data from the literature (Lit.)

Magmatic		Fe-Ti-P deposit		Andesite		Andesite (Lit.)		Granite (I-type)	
Geological setting		Fe-Ti-P deposit		Andesite		Andesite (Lit.)		Granite (I-type)	
Location	Bushveld Complex, South Africa	Bushveld Complex; Sept Iles, Canada ^a ; St. Charles de Bourget, Canada ^b	Lascar ^a and El Laco ^c stratovolcanoes, Northern Chile	Compilation from the literature		Opatica Subprovince, Canada			
Description	Massive mt, lowermost seams of the Upper Zone	Massive mt and massive nelsonite (mt + ap), uppermost seams of layered intrusions ^a Anorthosite-hosted massive nelsonite dyke ^b	Fresh calc alkaline lavas; glomerophenocrysts of mt, ap, pyroxene, plagioclase, and trace ilmenite	Mt phenocrysts in basaltic andesite, trachyandesite		Accessory magnetite in leucogranodiorite and leucotonalite protolith (orthogneiss)		No exsolutions	
Exsolutions in magnetite	Exsolutions of ilmenite and Mg-Al rich spinel	Exsolutions of ilmenite and Mg-Al rich spinel	Exsolutions of ilmenite rare						
References for sample locations	Barnes et al. (2004)	Barnes et al. (2004); Tollari et al. (2008); Nabil (2003); Martin-Tanguay (2012)	This study	This study		Grigsby (1990); Raziqigava and Naumova (1992); Audéat and Pettko (2006); Chiaradia et al. (2011)		Sawyer (2010)	
Source of data	This study	Méric (2011); This study	This study	This study		N=20		Potvin-Doucet (2012)	
Element and isotope	DL (33–75 μm)	N=4	N=11	N=3		N=20		N=6	
Si	EMP 20–130	Ave 514	Ave 137	Ave 490	Max 557	Ave 27,083	Ave 36,145	Ave 105	Min 63
Ca	EMP 23	Min 143	Min 24	Min 23	Min 23	Min 18,618	Min 13,414	Min 39	Min 24
Mg	0.01–0.1	Max 6,569	Max 9,480	Max 15,528	Max 17,221	Max 77,088	Max 158,857	Max 39	Max 30
Al	0.5–2.0	Min 13,511	Min 4,043	Min 6,647	Min 13,567	Min 13,414	Min 13,414	Min 670	Min 279
Si	27 500–3000	BDL	BDL	BDL	BDL	BDL	BDL	BDL	BDL
P	31 5–15	14	10	10	10	267	267	n.a.	n.a.
Sc	45 0.1–0.4	34	27	46	9	23	32	1.3	0.2
Ti	47 0.2–1.0	67,702	58,373	76,477	61,565	49,669	65,520	487	195
V	51 0.06–0.2	11,201	8,359	13,435	1,105	3,146	3,376	756	158
Cr	52 0.07–3.0	2,916	567	5,668	24	464	789	212	5
Mn	55 0.7–2.2	1,853	1,493	2,076	2,400	2,739	3,251	491	254
Co	59 0.05–0.2	212	100	281	28	196	241	35	21
Ni	60 0.4–1.6	489	391	590	6	148	496	34	22
Cu	63 0.04–0.1	42	5	137	4	11	103	12	5
Cu	65 0.15–0.7	45	9	140	2	12	103	15	10
Zn	66 0.2–0.8	471	318	666	301	667	871	452	334
Ga	71 0.1–0.4	42	28	48	41	47	52	47	31
Ge	74 0.15–0.5	0.76	0.53	0.86	0.69	0.40	0.60	n.a.	n.a.
Y	89 0.01–0.04	0.43	0.14	0.77	0.02	0.09	0.31	n.a.	n.a.
Zr	90 0.015–0.06	16	7	24	6	33	87	1.26	0.32
Zr	92 0.05–0.18	9	4	14	10	19	44	1.12	0.88
Nb	93 0.02–0.08	1.19	0.31	2.17	0.82	5.20	19.60	0.17	0.04
Mo	95 0.15–0.5	0.67	0.32	0.87	0.65	0.44	1.18	0.41	0.16
Sn	118 0.05–0.17	1.36	0.83	2.11	2.95	4.54	6.61	4.25	1.31
Hf	178 0.02–0.08	0.59	0.33	0.89	1.40	0.94	2.39	0.16	0.02
Ta	181 0.01–0.04	0.10	0.03	0.15	0.24	0.57	1.11	0.04	0.01
W	182 0.015–0.1	0.12	0.02	0.28	0.03	0.01	0.22	0.43	0.04
Pb	208 0.02–0.04	1.29	1.02	1.78	0.41	0.06	1.04	1112	4
Ni/Cr		0.29	0.09	0.69	0.16	0.29	0.63	0.86	0.17

Table 1 (continued)

Geological setting	High T hydrothermal (>500 °C)				Low T hydrothermal (<500 °C)			
	Magmatic	Felsic plutonic (Lit.)	High T hydrothermal (>500 °C)	IOCG deposit	Calcsic Fe-Skarn deposit	Banded Iron Formation	Carbonate alteration in serpentinite	
Location	Opatca Subprovinces, Canada	Compilation from the literature	Monococha-Surface, Peru	Ernest Henry, Australia	Vegas Peledas, Argentina	Pipe Mine, Thompson Ni Belt, Canada	Pipe Mine, Thompson Ni Belt, Canada	
Description	Accessory magnetite in leucogranodiorite and leucotonalite protolith (orthogneiss)	Accessory magnetite in granite, tonalite, granodiorite, quartz monazite	Disseminated magnetite in quartz veins (=K-feldspar, chalcopyrite, hematite) cutting hornfels and quartzmonzonite	Disseminated magnetite associated with pyrite, chalcopyrite, apatite, K-feldspar, quartz and calcite	Massive magnetite from retrograde exoskarn ^c	Banded Mt-chert-feldsparbiotite, trace pyrite. Pipe Formation (PI), host rock to komatiite	Disseminated Mt in carbonate vein in serpenitized komatiite	
Exsolutions in magnetite	No exsolutions	No exsolutions	No exsolutions	No exsolutions	No exsolutions	No exsolutions	Intergrown with dolomite	
References for sample locations	Sawyer (2010)	Grigsby (1990); Razjigaeva and Naumova (1992); Nadoll et al. (2012); Park et al. (2013)	Dupuis and Beaudoin (2011)	Dupuis and Beaudoin (2011)	Pons et al. (2009; sample VP2684b)	This study ^e	This study	
Source of data	Potvin-Doucet (2012)		Boutroy (unpublished)	Boutroy (unpublished)	This study	This study	This study	
Element and isotope	N=6	N=12	N=2	N=3	N=1	N=2	N=1	
Si	Max 148	Ave 1,052	Ave 365	Ave 126	Ave 9,748	Ave 349	Max 564	
Ca	65	Min 175	Min 267	Min 75	Min 6,589	Min 40	Ave 758	
Mg	57	Max 703	Max 510	Max 57	Max 1,462	Max 140	Max 60	
Al	1,333	Min 263	Min 1,818	Min 637	Min 9,066	Min 1,375	Ave 179	
Si	n.a.	Max 3,850	Max BDL	Max BDL	Max 9455	Max BDL	Max 2,058	
P	4.8	Ave 1,883	Ave 17	Ave n.a.	Ave 43	Ave n.a.	Ave n.a.	
Sc	1,054	Min 174	Min 2.34	Min 2.75	Min 0.15	Min 0.28	Ave 0.37	
Ti	1,299	Max 14,625	Max 2,285	Max 212	Max 709	Max 441	Ave 503	
V	497	Min 68	Min 765	Min 530	Min 36	Min 91	Ave 96	
Cr	663	Max 27,324	Max 75	Max 32	Max 10	Max 37	Ave 45	
Mn	51	Min 41	Min 659	Min 1,987	Min 1,076	Min 469	Ave 110	
Co	50	Max 82	Max 70	Max 13	Max 15	Max 11	Ave 3	
Ni	239	Min 0.2	Min n.a.	Min n.a.	Min 2.5	Min n.a.	Ave n.a.	
Cu	243	Max 24.1	Max 4.1	Max n.a.	Max 2.6	Max 0.9	Ave 1.0	
Zn	692	Min 384	Min 704	Min 49	Min 48	Min 33.8	Ave 53.4	
Ga	69	Max 15	Max 57	Max 29	Max 8.2	Max 8.2	Ave 12.4	
Ge	n.a.	Min 24	Min 1.23	Min 0.72	Min 2.0	Min 11.2	Ave 17.7	

Table 1 (continued)

Geological setting	Magmatic		High T hydrothermal (>500 °C)				Low T hydrothermal (<500 °C)					
	Granite (I-type)	Felsic plutonic (Lit.)	High T hydrothermal (>500 °C)	IOCG deposit	Calciic Fe-Skarn deposit	Banded Iron Formation	Carbonate alteration in serpentinite	High T hydrothermal (>500 °C)	IOCG deposit	Calciic Fe-Skarn deposit	Banded Iron Formation	Carbonate alteration in serpentinite
Y	n.a.		0.16	0.09	0.23	0.04	0.01	0.06	1.64	0.33	0.11	0.56
Zr	2.48		n.a.	n.a.	n.a.	n.a.	n.a.	n.a.	2.23	n.a.	n.a.	n.a.
Zr	1.65		0.20	0.09	0.31	0.48	0.09	1.17	1.43	0.20	0.07	0.33
Nb	0.38		0.19	0.04	0.33	0.02	0.01	0.02	0.18	0.33	0.10	0.56
Mo	0.92		0.94	0.65	1.24	0.41	0.11	0.93	0.44	1.19	0.39	1.99
Sn	13.69		3.34	2.55	4.14	1.24	0.48	2.35	1.03	0.74	0.56	0.91
Hf	0.41		0.02	0.01	0.03	0.07	0.00	0.21	0.1	0.01	0.01	0.02
Ta	0.10		0.03	0.03	0.04	0.01	0.01	0.01	0.03	0.03	0.01	0.06
W	1.30		0.20	0.05	0.36	0.15	0.04	0.28	1.36	0.09	0.08	0.11
Pb	2656		n.a.	n.a.	n.a.	n.a.	n.a.	n.a.	n.a.	n.a.	n.a.	n.a.
Ni/Cr	5.42	0.06	13.78	2.49	25.08	8.14	1.00	15.13	13.93	0.41	0.27	0.54

Between three and eight grains were analyzed in each sample. Minimum and maximum detection limits (DL) correspond to the largest (75 μm) and smallest (33 μm) beam size, respectively. ⁹²Zr and ⁶³Cu are the preferred isotopes (see explanation of interferences in the [Electronic Appendix](#))

^c Temperature of fluids that formed this sample are calculated by Pons et al. (2009) as <320 °C and were a mix of magmatic fluids with meteoritic fluids

^d Location of andesite from Northern Chile: Blocky andesite lava flow (Stage 1 of Gardeweg et al. (1998)) from Lascar volcano (23° 22' S, 67° 44' W)

^e Vale borehole (see Layton-Matthews et al. 2007 for general description of Thompson Ni Belt)

T temperature, *Lit.* Literature data, *Mt* magnetite, *Ap* apatite, *IOCG* iron oxide copper gold, *N* number of samples, *EMP* electron microprobe, *BDL* below detection limit

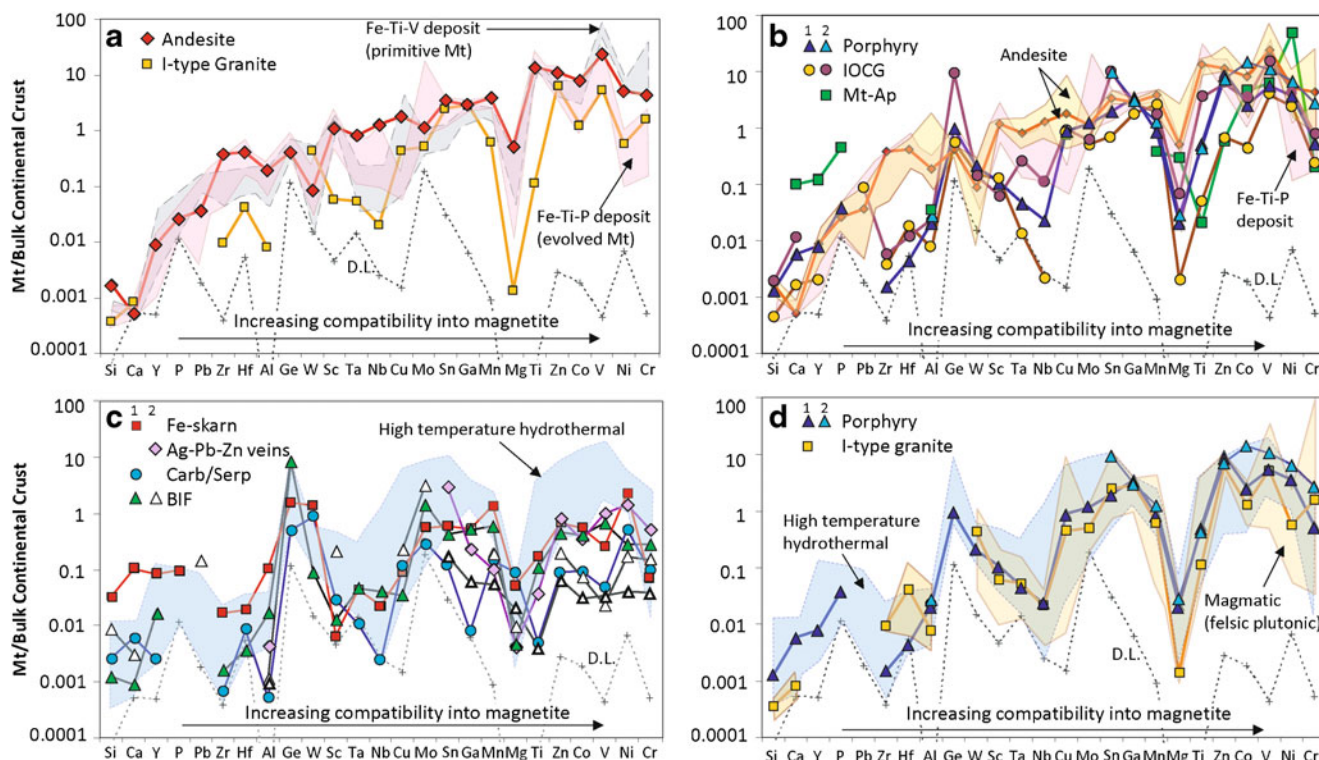


Fig. 1 Multielement variation diagrams for magnetite (*Mt*), normalized to bulk continental crust (values from Rudnick and Gao 2003), from a wide range of environments (see Table 1 for details). D.L. minimum detection limit for 75- μm beam size. **a** Magmatic magnetite from intermediate magmas (Fe-Ti-V deposits; *gray field* (Bushveld Complex, S. Africa), Fe-Ti-P deposits; *pink field* (Sept Iles, Canada; St. Charles de Bourget, Canada; Bushveld Complex), and andesite lavas) and felsic magmas (I-type granite) analyzed in this study. For clarity, only average values of andesite (northern Chile) and granite (Opatica, Canada) are shown. Full range of magnetite data (both this study and literature compiled in Table 1) for andesite (*yellow field*) and felsic plutonic rocks (*orange field*) are plotted in **(b)** and **(d)**, respectively. **b** Magnetite from high-temperature (>500 °C) magmatic-hydrothermal deposits (1 this study and 2 literature): porphyry-Cu (1 Morococha, Peru and 2 review of Nadoll et al. (2014)) and IOCG (1 Ernest Henry, Australia; 2 Bafq, Iran; Bonyadi et al. (2011)) deposits; compared to Mt from intermediate

magmas (Fe-Ti-P deposit; *pink field* and andesite; *orange field*). Low-temperature (~300 °C) hydrothermal magnetite-apatite (Ap) from 2 Othrys ophiolite (Mitsis and Economou-Eliopoulos 2001) plotted for comparison. **c** Magnetite from low-temperature (<500 °C) environments (1 this study and 2 literature): retrograde Fe-skarn (1 Vegas Peledas, Argentina), Ag-Pb-Zn veins (2 Coeur d'Alene, USA; Nadoll et al. (2012, 2014)), disseminated magnetite in carbonate (Carb) veins in serpentinite (Serp: 1 Thompson Ni-belt, Canada), and Banded Iron Formation (BIF: 1 Thompson Ni-Belt, Canada; 2 Dales Gorge, Australia; Pecoits et al. (2009)); 2 BIF compilation of Nadoll et al. (2014)); compared with Mt from high-temperature hydrothermal deposits, such as IOCG and porphyry-Cu, (*blue field* drawn from data in 1b with additional data from Boutroy (2014), total of six deposits). **d** Range of magnetite from high-temperature hydrothermal deposits (*blue field*) compared to magmatic Mt from arc-related felsic plutonic rocks (*orange field*)

continental crust, rather than to another magnetite (c.f. Nadoll et al. 2012, 2014), in order to approximate the composition of the liquid (or fluid) from which magnetite is formed. We chose bulk continental crust because (a) it is closer in composition to an evolved silicate melt (saturated in magnetite), such as ferrodiorite, than primitive mantle (undersaturated in magnetite), and (b) hydrothermal fluids are more likely to have interacted with crustal rocks rather than primitive mantle. As a result, the normalized pattern of magmatic magnetite, such as that from andesite (Fig. 1a), increases from left (lower values for elements incompatible into magnetite) to right (higher values for elements compatible into magnetite). Thus, any differences in the shape of the magnetite pattern should reflect different abundances of trace elements in the liquid and/or differences in the partition coefficient of magnetite, for example due to different conditions of oxygen

fugacity, temperature, or cooling rate. Moreover, anomalies in the pattern due to competition for an element among phases co-crystallizing with magnetite (e.g., ilmenite and sulfide) are more readily observed. Although there are many complex factors which influence the trace element abundance in magnetite, magnetite from environments with similar physicochemical conditions should be similar in composition, whereas those formed under different conditions will be different, thus resulting in distinctive chemical signatures which could aid in discrimination of magnetite from different environments (Dupuis and Beaudoin 2011; Nadoll et al. 2014).

Magnetite from silicate melts

Magmatic Fe-oxide deposits are an important source of Ti (in ilmenite), V (in magnetite), and P (in apatite). They commonly

form from evolved silicate melt (~ferrodiorite in composition) at the top of layered intrusions which, for the intrusions studied (Bushveld Complex and Sept Iles), are associated with plume-related magmas in a rift environment (Higgins 2005; Barnes et al. 2010). The concentration of elements that are compatible during fractionation (i.e., V and Cr) are commonly used in magnetite to trace the evolution of the melt and identify reinjection of primitive melt and magma mixing (e.g., McCarthy and Cawthorn 1983; Barnes et al. 2004; Tegner et al. 2006; Namur et al. 2010). In the Bushveld Complex and Sept Iles layered intrusions, Ti-rich magnetite (6–12 wt.% Ti) crystallized before or at the same time as ilmenite under relatively oxidizing (~quartz-fayalite-magnetite (QFM) buffer) conditions (Toplis and Carroll 1995; Toplis and Corgne 2002; Namur et al. 2010). Oxygen fugacity controls the V content of magnetite with the maximum value of D_v into magnetite occurring at ~QFM (Toplis and Corgne 2002). Thus, the first magnetite to crystallize in these layered intrusions are V-rich (0.8–1.4 wt.% V), and the V content of magnetite steadily decreases up section with the last magnetite, crystallizing at the very end of fractionation together with apatite (Fe-Ti-P deposit), typically V-poor (e.g., Barnes et al. 2004). In contrast, the first magnetite to crystallize under either higher or lower f_{O_2} conditions is V-poor (<0.8 wt.%) because D_v between magnetite and melt is lower (Toplis and Corgne 2002).

In order to illustrate the effect fractionation of a silicate melt has on the trace element content of magnetite (Fig. 1a), we analyzed Fe-oxides from (a) the lowermost and uppermost layers of massive magnetite (Fe-Ti-V and Fe-Ti-P deposits, respectively) in the upper zone of the Bushveld Complex, which are separated by a stratigraphic thickness of 1.3 km (Barnes et al. 2004); (b) the base (massive mineralization) to the top (disseminated mineralization) of the Fe-Ti-P deposit (200-m thickness) in the most evolved part of Sept Iles layered intrusion (Tollari et al. 2008; Méric 2011); and (c) a massive magnetite-apatite dyke of St. Charles de Bourget associated with the anorthosite of Lac St. Jean, Canada (Martin-Tanguay 2012). The behavior of trace elements during fractionation is recorded in both magnetite and ilmenite in each layered intrusion as follows (Fig. 1a), although ilmenite is significantly enriched in Ti, Hf, Mg, Mn, Nb, Sc, Ta, W, and Zr relative to coexisting magnetite (Méric 2011). Elements compatible (Mg, Ni, Co, V, and Cr) during crystallization of olivine, pyroxene, and magnetite itself are most concentrated in more primitive magnetite from the lowermost layers and decrease up section. Elements that are incompatible during fractionation (Ga, Ge, Hf, Mn, Mo, Nb, Sc, Sn, Ta, Ti, W, Zn, and Zr) show the inverse and increase up section and are most concentrated in more evolved magnetite in the uppermost parts of the intrusions (Méric 2011). Aluminium shows no significant variation up section. In the absence of magmatic sulfides (i.e., sulfide undersaturated magmas), Cu (highly chalcophile) is also incompatible during fractionation and should also increase in

magnetite up section. However, trace amounts of cumulus magmatic sulfides are present in the Fe-Ti-P samples from the Bushveld (Barnes et al. 2004) and Sept Iles (Nabil 2003). This is common towards the end of fractionation in many layered intrusions and can be triggered by crystallization of magnetite itself (Maier et al. 2003). Co-crystallization of magnetite and sulfide liquid results in depletion of Cu in magnetite relative to other incompatible elements such as Nb and Mo (Fig. 1a) and is, thus, indicative of sulfide saturation of magma. The remaining elements, Si, Ca, P, Y, and Pb, show no significant variation in magnetite during fractionation. These elements are the most incompatible into magnetite so that any variation in the silicate liquid during fractionation is not obviously recorded by magnetite. Magnetite from all three Fe-Ti-P deposits, hosted in different intrusions, have relatively similar trace element patterns (pink field, Fig. 1a). However, there is some overlap between the magnetite patterns of Fe-Ti-P and Fe-Ti-V deposits (gray field, Fig. 1a), and thus only a few critical elements (i.e., Cr, Ni, V \pm Ti, Mo, Nb, and Ta) can discriminate between them. The crystallization of ilmenite before magnetite also affects magnetite composition. In some anorthosite-hosted Fe-oxide deposits, this results in magnetite relatively depleted in elements that preferentially partition into early-forming ilmenite, i.e., Ti (2–6 wt.%), Hf, Mg, Mn, Nb, Sc, Ta, W, and Zr (Néron 2012).

Fresh andesite samples from the volcanoes of Lascar and El Laco (N. Chile) contain phenocrysts of magnetite and apatite (ilmenite is scarce). Magnetite is Ti-rich (6 wt.% Ti) and similar in composition to magnetite from other arc-related intermediate rocks (Table 1 and Fig. 1b). Its trace element pattern is also similar to magnetite from plume-related Fe-Ti-P deposits, except for higher Ni, Cr, and Cu contents (Fig. 1a). These andesite samples are from a moderately oxidized arc magma (+2 QFM), as calculated using magnetite-ilmenite equilibrium following the method of Andersen and Lindsley (1985) and Lepage (2003), which was probably sulfide undersaturated because under these oxidizing conditions sulfate rather than sulfide is stable (Jugo et al. 2010). As a result, magnetite contains some Cu (30–100 ppm; Table 1) in solid solution and shows no Cu depletion relative to Nb and Mo (Fig. 1a).

Magnetite in I-type granite represents the composition of magmatic magnetite crystallizing from extreme degrees of fractionation. Although partition coefficients between mineral and melt generally increase with increasing Si content of the magma magnetite from granite contains the lowest overall abundance of trace elements among all the studied magmatic magnetite (Fig. 1a). They are similar to some extent to magnetite from evolved mafic melts (i.e., similar low concentrations of Cr, Ni, V, and Co), but contain much lower concentrations of Ti (<0.5 wt.%), Mg, Mn, Nb, Sc, Al, Zr, and Hf, and exsolutions of ilmenite are absent. This most likely reflects (1) the low abundance of certain incompatible elements

probably after the saturation of accessory phases in the melt, such as titanite (for Ti and Nb) and zircon (Zr and Hf), which are present in the samples studied (Sawyer 2010), and (2) the low abundance of compatible elements in an evolved felsic melt. Magnetite depleted in Ti, Al (both <1 wt.%), and Mg (<0.1 wt.%), with an absence of ilmenite exsolutions, is common in felsic rocks (Grigsby 1990; Nadoll et al. 2012; see compilation of previously published data in Table 1).

Magnetite from sulfide melts

The composition and behavior of trace elements in magnetite crystallizing from a sulfide melt is different from that crystallizing from silicate melt because (a) the sulfide melt is enriched in chalcophile elements (such as Ni, Cu, and PGE), whereas the silicate melt is enriched in lithophile elements, and (b) the co-crystallizing phases are different. As silicate minerals do not crystallize from the sulfide melt, all of the lithophile elements, albeit in low abundance in the sulfide melt, are concentrated in magnetite and controlled solely by its crystallization throughout fractionation (Dare et al. 2012; Boutroy et al. 2014). Early-forming magnetite in Fe-rich sulfide cumulates is enriched in all of the lithophile elements (<2 wt.% Ti, V, and Cr), which become gradually depleted in the residual melt so that magnetite crystallizing late from the residual Cu-rich sulfide liquid contains the lowest concentrations of all these elements (<50 ppm). Of the chalcophile

elements, only Ni, Co, Zn, Sn, and Mo are present in magnetite, the concentration of which depends on competition from co-crystallizing sulfides (Fe-Ni-rich monosulfide solid solution or Cu-rich intermediate solid solution) in addition to the concentration of these elements in the sulfide liquid (Dare et al. 2012; Boutroy et al. 2014).

Magnetite in hydrothermal systems

The comprehensive review of Nadoll et al. (2014) for hydrothermal magnetite and host igneous porphyry magnetite discusses in detail the various factors that most likely control trace elements in magnetite from a wide range of hydrothermal environments. Although experimental data is lacking for the partitioning of trace elements between magnetite and fluids, Nadoll et al. (2014) consider that the same factors controlling trace elements in magnetite at igneous conditions (fluid/melt composition, temperature, pressure, cooling rate, oxygen fugacity, sulfur fugacity, and silica activity) should apply equally to magnetite from lower-temperature hydrothermal conditions, with the additional parameter of fluid-host rock interaction.

Examples of hydrothermal magnetite (data from this study and that published in the literature) are plotted on the multi-element diagram (Fig. 1b–d), using the same order of partition coefficients used for magmatic magnetite, to illustrate in most

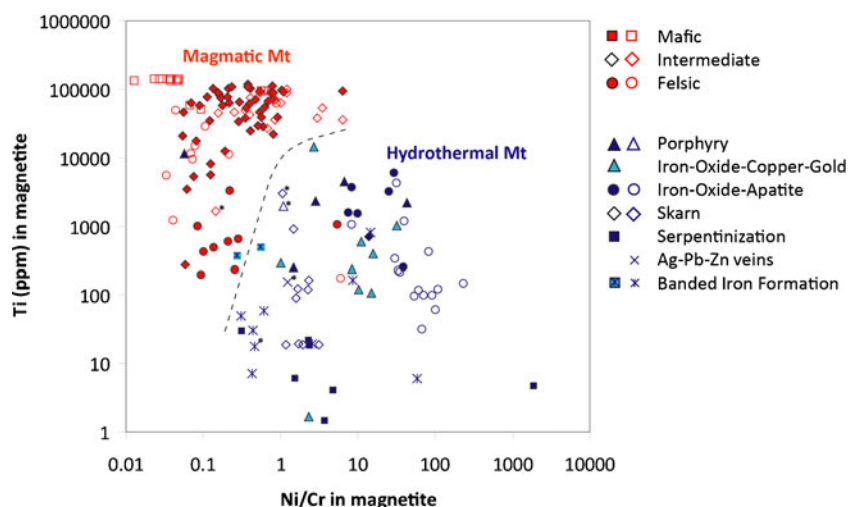


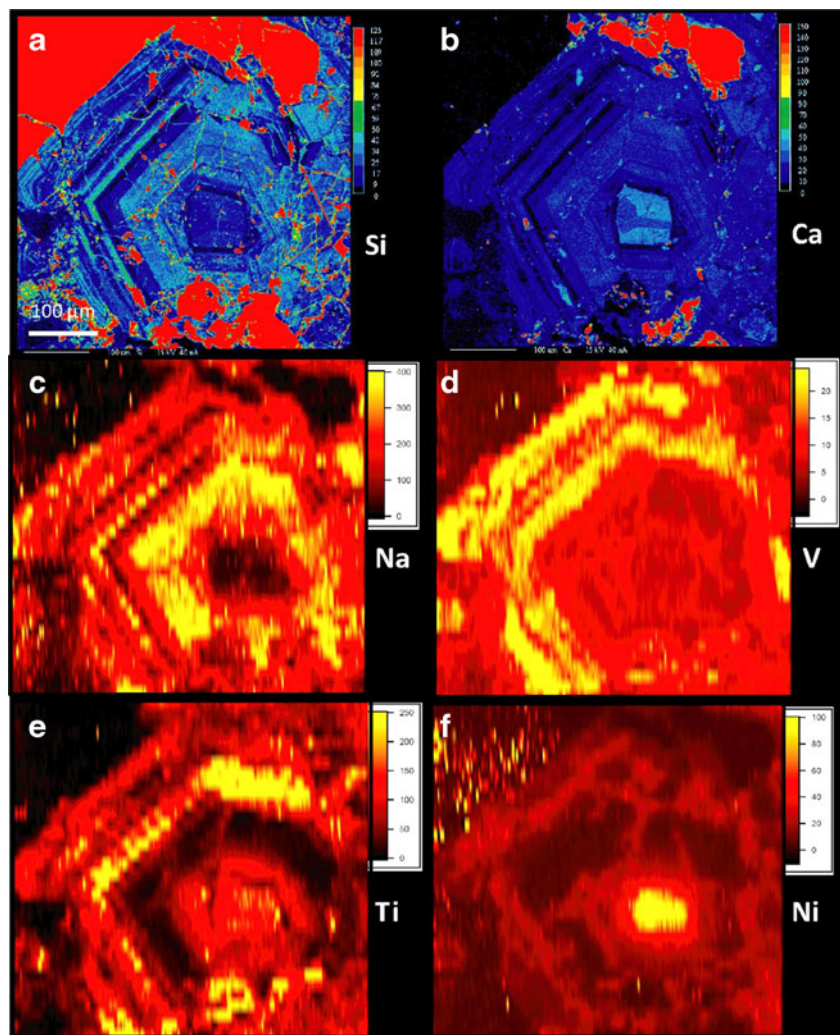
Fig. 2 Plot of Ti (ppm) versus Ni/Cr ratio (un-normalized) in magnetite (mt) to distinguish magmatic (red) and hydrothermal (blue) settings. Solid symbols data from this study (Table 1) with additional LA-ICP-MS data from Méric (2011), Sept Iles Intrusion; Néron (2012), Fe-Ti ± P mineralization, Anorthosite of Lac St. Jean, Quebec; Potvin-Doucet (2012), S-type granite, Wuluma, Australia; and Boutroy (2014)—analysis of samples of porphyry-Cu (Porgera, Bajo, Ridgeway, Reko Diq), IOCG (Kwiyibo, Guelb Moghrein), and IOA (Kiruna, El Romeral, Pea Ridge, Pilot Knob, Rektor, Savage River) from Dupuis and Beaudoin (2011). Magnetite from Fe-Ti-V and -P deposits are plotted as intermediate compositions. Open symbols data from the literature (EMP and LA data):

Variety of mafic, felsic, and intermediate rocks (Razjigaeva and Naumova 1992); basalt (Gregory 2006); andesite (Chiaradia et al. 2011); felsic plutonic (Nadoll et al. 2012, 2014; Park et al. 2013); Fe-Ti-V deposit (Liu et al. 2014); iron-oxide-copper-gold (Bonyadi et al. 2011); porphyry-Cu (Nadoll et al. 2014); iron-oxide-apatite (Nyström and Henriquez 1994; Mitsis and Economou-Eliopoulos 2001); skarn (Dupuis and Beaudoin 2011; Nadoll et al. 2014); Ag-Pb-Zn veins (Nadoll et al. 2014); and banded iron formation (Bhattacharya et al. 2007; Angerer et al. 2012; Nadoll et al. 2014). Each symbol is an individual sample except for those marked with an asterisk, which are median values of a large database compiled in the review of Nadoll et al. (2014)

cases how different the patterns are for magnetite from different environments, reflecting differences in fluid composition, physiochemical parameters, and possibly even partition coefficients. The multielement diagram reveals that hydrothermal magnetites have distinctly different, and more varied, chemical signatures to magnetite from intermediate magmas (Fig. 1b, c). Not only is hydrothermal magnetite depleted in Ti (<2 wt.%) and Al (<1 wt.%), as previously demonstrated (Ray and Webster 2007; Dupuis and Beaudoin 2011; Nadoll et al. 2012; Nadoll et al. 2014), but also in other high field strength elements (Zr, Hf, Nb, Ta, and Sc). All of these elements are considered relatively immobile during hydrothermal alteration (van Baalen 1993) and thus are present at low concentrations in most hydrothermal fluids. For Ti, which is compatible in magnetite, this confirms that the fluid from which magnetite precipitated was impoverished in these immobile elements. Magnetite forming from high-temperature hydrothermal fluids (~500–700 °C) associated with a magmatic-hydrothermal source (e.g., porphyry and IOCG deposits) is typically enriched in Ni, V, Co, Zn, Mn, and Sn

almost to the same concentrations as magnetite from evolved intermediate magmas (Fig. 1b) that crystallize apatite together with magnetite (e.g., andesite and Fe-Ti-P deposits). As these transition metals are typically compatible in magnetite, their abundance in hydrothermal magnetite indicates that they were present in the fluid because they are commonly mobile during alteration. This is confirmed by the presence of Mn and Zn (100–1,000 ppm) commonly measured in fluid inclusions from porphyry-Cu (Baker et al. 2004) and IOCG (Rusk et al. 2010) deposits. Although Cu and Pb are also common in these types of hydrothermal fluids, they are in relatively low abundance in magnetite possibly due to the competition of magnetite with the precipitation of sulfides (for Cu) and the incompatible nature of Pb into magnetite. Even Ni and Co, together with Cu, have been detected in arc-related volcanic gasses (Nadeau et al. 2010), where it is thought that magmatic hydrothermal fluids can derive their metals from dissolution of sulfide melt droplets during injection of reduced mafic magma (sulfide-bearing) into oxidized felsic magma (Keith 1997; Larocque et al. 2000).

Fig. 3 Chemical maps of zoned magnetite from Fe-skarn of Vegas Peledas by electron microprobe (a, b: beam size 3 μm) and LA-ICP-MS (c, f: beam size 15 μm). All elements display euhedral, oscillatory zoning: Al, Mg, and Ga is similar to Ca; K and Zn similar to Na; Mn most similar to V; and Zr and Nb similar to Ni. Color scale for LA-ICP-MS maps is in ppm



Compared to high-temperature hydrothermal magnetite (Fig. 1c), magnetite forming from lower-temperature fluids (<500 °C), in both hydrothermal (e.g., retrograde Fe-skarn) and sedimentary (e.g., BIF) environments, are notably depleted in these compatible elements probably due to low solubility of these elements in fluids at lower temperatures (Ray and Webster 2007; Nadoll et al. 2012, 2014). As a result, they have the lowest overall abundance of trace elements, making them clearly distinct from both magmatic and high-temperature hydrothermal magnetite by their overall flatter normalized patterns, except for relative enrichment in Ge and W in some cases (Fig. 1c). However, the temperature of hydrothermal deposition of magnetite and apatite in the mantle shear zone of the Othrys ophiolite in Greece is also low (~300 °C; Mitsis and Economou-Eliopoulos 2001, 2003), but its magnetite has high Ni, V, and Co contents, similar to those from high-temperature environments, in addition to unusually high Mg (Fig. 1b). This illustrates the importance also of the country rock as a source of trace elements, with elevated concentrations of Ni, Mg, and Co probably leached from mafic-ultramafic rocks under certain physiochemical conditions (e.g., Pecoits et al. 2009).

An important difference between magmatic and hydrothermal magnetite is the behavior of Ni and Cr. In silicate magmas, their behavior is coupled, with Ni/Cr ratios ≤ 1 , as both behave compatibly during fractionation of intermediate and felsic melts (Fig. 1a). However, in many hydrothermal settings (Fig. 1b, c), their behavior is decoupled and the Ni/Cr ratio of magnetite is typically higher (≥ 1 ; Fig. 2), probably due to a higher solubility of Ni compared to Cr in fluids. This difference in behavior of Ni/Cr in fact appears to be the only way to distinguish magnetite from high-temperature hydrothermal deposits and felsic host rocks (such as I-type granite), which otherwise have very similar trace element signatures (Fig. 1d). Thus, a plot of Ti versus Ni/Cr (Fig. 2) can be used to discriminate magnetite between hydrothermal and all magmatic environments.

Elements that are incompatible into magnetite (Si and Ca) and typically absent in magmatic magnetite can be enriched in magnetite from some hydrothermal settings (Fig. 1b, c). Silica and Ca were determined by electron microprobe (beam size 5–10 μm) to avoid any visible silicate inclusions. Si-rich magnetite (0.1–6 wt. % Si) is reported to only form by a special precipitation mechanism from hydrothermal solutions, which is not yet understood but is most common in skarns, some of which may also contain appreciable amounts of Ca (0.1–1 wt.%), and is uncommon in most other igneous and hydrothermal settings (Shimazaki 1998). In a few cases, Si-rich magnetite is zoned with the shape of the silica-bearing zone taking the same form as the crystal habit, indicating a change in the conditions during crystal growth (Shimazaki 1998). Similar oscillatory zonation is present in Si-rich magnetite (<1.6 wt.%) from Fe-skarn in this study (Fig. 3), where

laser ablation–ICP-MS mapping illustrates that not only Si but all elements, including those that are relatively immobile and in low abundance (e.g., Ti), vary from one zone to another. This zonation most likely represents changes in fluid composition and/or physiochemical parameters (such as temperature, pH, and perhaps even redox conditions), that could also periodically change the partitioning behavior of trace elements into magnetite during its precipitation. However, it cannot be ruled out that the Si-rich zone could be due to micro-nanoscale inclusions incorporated during certain periods of magnetite growth.

Conclusions

We present a coherent explanation for the behavior of trace element partitioning in magnetite during crystallization from silicate melts and hydrothermal fluids in a variety of ore deposits. This is based on a new multielement variation diagram for 25 trace elements, determined by laser ablation ICP-MS, using data generated in this study and previously published in the literature. We show that the chemical patterns of magnetite from different environments (magmatic, high-temperature magmatic hydrothermal, and low-temperature hydrothermal) are distinct and are controlled by the composition of the melt/fluid, co-crystallizing phases, and physiochemical parameters such as temperature and oxygen fugacity. This new diagram could be applied to petrogenetic and provenance studies, in particular in the exploration of ore deposits.

Acknowledgments This project was funded by NSERC, DIVEX, Vale, and the Canadian Research Chair in Magmatic Metallogeny. We thank S. Medhi, D. Savard, and M. Choquette for their assistance with laser ablation-ICP-MS and microprobe analyses and F. Tomos for andesite samples from Chile. Comments by E. Sawyer and D. Gaboury helped improve the paper at an early stage. We thank the Editors (A. Barth and R. Cox) and reviewers of *Geology* (K. Goodenough, J. Mauk, and 1 anonymous) for their useful comments which helped improve an early version of this manuscript. Thanks are also given to P. Nadoll and B. Lehmann for their reviews and editorial handling of this manuscript in *Mineralium Deposita*.

References

- Andersen D, Lindsley D (1985) New (and final!) models for the Ti-magnetite/ilmenite geothermometer and oxygen barometer. *Eos Trans AGU* 66:416
- Angerer T, Hagemann SG, Danyushevsky L (2012) Geochemical evolutions of the banded iron formation-hosted high-grade iron ore system in the Koolyanobbing Greenstone Belt, Western Australia. *Econ Geol* 107:599–644
- Angerer T, Hagemann SG, Danyushevsky L (2013) High-grade iron ore at Windarling, Yilgarn Craton: a product of syn-orogenic deformation, hypogene hydrothermal alteration and supergene modification in an Archean BIF-basalt lithostratigraphy. *Miner Deposita* 48:697–728

- Audetat A, Pettke T (2006) Evolution of a porphyry-Cu mineralized magma system at Santa Rita, New Mexico (USA). *J Petrol* 47: 2021–2046
- Baker T, Van Achterberg E, Ryan CG, Lang JR (2004) Composition and evolution of ore fluids in a magmatic-hydrothermal skarn deposit. *Geol* 32:117–120
- Barnes S-J, Maier WD, Ashwal LD (2004) Platinum-group element distribution in the Main Zone and Upper Zone of the Bushveld Complex, South Africa. *Chem Geol* 208:293–317
- Barnes S-J, Maier WD, Curl EA (2010) Composition of the marginal rocks and sills of the Rustenburg Layered Suite, Bushveld Complex, South Africa: implications for the formation of the platinum-group element deposits. *Econ Geol* 105:1491–1511
- Bhattacharya HN, Chakraborti I, Ghosh KK (2007) Geochemistry of some banded iron-formations of the Archean supracrustals, Jharkhand-Orissa region, India. *J Earth Syst Sci* 116:245–259
- Bonyadi Z, Davidson GJ, Mehrabi B, Meffre S, Ghazban F (2011) Significance of apatite REE depletion and monazite inclusions in the brecciated Se-Chahun iron oxide-apatite deposit, Bafq district, Iran: insights from paragenesis and geochemistry. *Chem Geol* 281: 253–269
- Boutroy E, Dare SAS, Beaudoin G, Barnes S-J, Lightfoot PC (2014) Magnetite composition in Ni-Cu-PGE deposits worldwide and its application to mineral exploration. *J Geochem Explor* doi:10.1016/j.gexplo.2014.05.010
- Chiaradia M, Müntener O, Beate B (2011) Enriched basaltic andesites from mid-crustal fractional crystallization, recharge, and assimilation (Pilavo Volcano, Western Cordillera of Ecuador). *J Petrol* 52: 1107–1141
- Dare SAS, Barnes S-J, Beaudoin G (2012) Variation in trace element content of magnetite crystallized from a fractionating sulfide liquid, Sudbury, Canada: implications for provenance discrimination. *Geochim Cosmochim Acta* 88:27–50
- Dupuis C, Beaudoin G (2011) Discriminant diagrams for iron oxide trace element fingerprinting of mineral deposit types. *Miner Deposita* 46: 319–335
- Gardegweg MC, Sparks RSJ, Matthews SJ (1998) Evolution of Lascar volcano, northern Chile. *J Geol Soc* 155:89–104
- Gregory MJ (2006) Copper mobility in the Eastern Creek Volcanics, Mount Isa, Australia: evidence from laser ablation ICP-MS of iron-titanium oxides. *Miner Deposita* 41:691–711
- Grigsby JD (1990) Detrital magnetite as a provenance indicator. *J Sediment Res* 60
- Higgins MD (2005) A new interpretation of the structure of the Sept Iles Intrusive suite, Canada. *Lithos* 83:199–213
- Jugo PJ, Wilke M, Botcharnikov RE (2010) Sulfure K-edge XANES analysis of natural and synthetic basaltic glasses: implications for S speciation and S content as function of oxygen fugacity. *Geochim Cosmochim Acta* 74:5926–6938
- Keith JD (1997) The role of magmatic sulfides and mafic alkaline magmas in the Bingham and Tintic mining districts, Utah. *J Petrol* 38:1679–1690
- Larocque AC, Stimac JA, Keith JD, Huminicki MAE (2000) Evidence for open-system behavior in immiscible Fe-S-O liquids in silicate magmas: implications for contributions of metals and sulfur to ore-forming fields. *Can Mineral* 38:1233–1250
- Layton-Matthews D, Leshar CM, Burnham OM, Liwanag J, Halden NM, Hulbert L, Peck DC (2007) Magmatic Ni-Cu-platinum-group element deposits of the Thompson Nickel Belt. *Mineral Deposits of Canada: A synthesis of major deposit-types, District Metallogeny, the evolution of geological provinces, and exploration methods* Edited by WD Goodfellow Geological Association of Canada, Mineral Deposits Division, Special Publication 5:409–432
- Lepage LD (2003) ILMAT: an Excel worksheet for ilmenite-magnetite geothermometry and geobarometry. *Comput Geosci* 29:673–678
- Liu P-P, Zhou M-F, Chen WT, Boone M, Cnudde V (2014) Using multiphase solid inclusions to constrain the origin of the Baima Fe-Ti-(V) oxide deposit, SW China. *J Petrol* 55:951–976
- Maier WD, Barnes S-J, Gartz V, Andrews G (2003) Pt-Pd reefs in magnetites of the Stella layered intrusion, South Africa: a world of new exploration opportunities for platinum group elements. *Geology* 31:885–888
- Martin-Tanguay B (2012) Pétrographie et caractérisation des oxydes de Fe-Ti à Saint-Charles de Bourget (Québec), associé à la suite anorthositique du Lac-Saint-Jean. Université du Québec à Chicoutimi, pp 71
- McCarthy T, Cawthorn RG (1983) The geochemistry of vanadiferous magnetite in the Bushveld complex: implications for crystallization mechanisms in layered complexes. *Miner Deposita* 18:505–518
- Méric J (2011) Caractérisation géochimiques des magnétites de la zone critique de l'intrusion magmatique de Sept-Iles (Québec, Canada) et intégration à une base de données utilisant la signature géochimique des oxydes de fer comme outil d'exploration Université du Québec à Chicoutimi - Université Montpellier 2, pp 48
- Mitsis I, Economou-Eliopoulos M (2001) Occurrence of apatite associated with magnetite in an ophiolite complex (Othrys), Greece. *Am Mineral* 86:1143–1150
- Mitsis I, Economou-Eliopoulos M (2003) On the origin of hydroxylapatite associated with pure massive magnetite in the Othrys Ophiolite Complex, Greece. *Ofioliti* 28:25–32
- Mollo S, Putirka K, Iezzi G, Scarlato P (2013) The control of cooling rate on titanomagnetite composition: implications for a geospeedometry model applicable to alkaline rocks from Mt. Etna volcano. *Contrib Mineral Petrol* 165:457–475
- Nabil H (2003) Genèse des dépôts de Fe-Ti-P associés aux intrusions litées (exemples: l'intrusion mafique de Sept-Iles, au Québec; complexe de Duluth aux États-Unis). Université du Québec à Chicoutimi, pp 537
- Nadeau O, Williams-Jones AE, Stix J (2010) Sulphide magma as a source of metals in arc-related magmatic hydrothermal ore fluids. *Nat Geosci* 3:501–505
- Nadoll P, Mauk JL, Hayes TS, Koenig AE, Box SE (2012) Geochemistry of magnetite from hydrothermal ore deposits and host rocks of the Mesoproterozoic Belt Supergroup, United States. *Econ Geol* 107: 1275–1292
- Nadoll P, Angerer T, Mauk JL, French D, Walshe J (2014) The chemistry of hydrothermal magnetite: a review. *Ore Geol Rev* 16:1–32
- Namur O, Charlier B, Toplis MJ, Higgins MD, Liégeois J-P, Vander Auwera J (2010) Crystallization sequence and magma chamber processes in the ferrobaltic Sept Iles layered intrusion, Canada. *J Petrol* 51:1203–1236
- Néron A (2012) Caractérisation géochimiques des oxydes de Fe-Ti dans un dépôt de Fe-Ti-P associé à la suite anorthositique de Lac Saint Jean, Québec, Canada (secteur Lac à Paul) et intégration des données du secteur Lac à La Mine. Université du Québec à Chicoutimi, pp 39
- Nyström J, Henriquez F (1994) Magmatic features of iron ores of the Kiruna type in Chile and Sweden: ore textures and magnetite geochemistry. *Econ Geol* v:89
- Park J-W, Campbell IH, Ickert RB, Allen CM (2013) Chalcophile element geochemistry of the Boggy Plain zoned pluton, southeastern Australia: a S-saturated barren compositionally diverse magmatic system. *Contrib Mineral Petrol* 165:217–236
- Pecoits E, Gingras M, Barley M, Kappler A, Posth N, Konhäuser K (2009) Petrography and geochemistry of the Dales Gorge banded iron formation: paragenetic sequence, source and implications for palaeo-ocean chemistry. *Precambrian Res* 172:163–187
- Pons JM, Franchini M, Meinert L, Recio C, Etcheverry R (2009) Iron skarns of the Vegas Peladas District, Mendoza, Argentina. *Econ Geol* 104:157–184

- Potvin-Doucet C (2012) Distribution et comparaison d'éléments traces dans la magnétite contenue dans des granites de types I et S Sciences de la terre. Université du Québec à Chicoutimi, pp 43
- Ray G, Webster I (2007) Geology and chemistry of the low Ti magnetite-bearing Heff Cu-Au skarn and its associated plutonic rocks, Heffley Lake, south-central British Columbia. *Explor Min Geol* 16:159–186
- Razjigaeva N, Naumova V (1992) Trace element composition of detrital magnetite from coastal sediments of northwestern Japan Sea for provenance study. *J Sediment Res* 62:802–809
- Reguir EP, Chakhmouradian AR, Halden NM, Yang P, Zaitsev AN (2008) Early magmatic and reaction-induced trends in magnetite from the carbonatites of Kerimasi, Tanzania. *Can Mineral* 46:879–900
- Rudnick R, Gao S (2003) Composition of the continental crust. *Treatise Geochem* 3:1–64
- Rusk B, Oliver N, Cleverley J, Blenkinsop T, Zhang D, Williams P, Habermann P (2010) Physical and chemical characteristics of the Ernest Henry iron oxide copper gold deposit, Australia: implications for IOGC genesis. In: Porter T (ed) *Hydrothermal iron oxide copper-gold and related deposits: a global perspective, v 3—advances in the understanding of IOGC deposits*. PGC Publishing, Adelaide, pp 201–218
- Sawyer E (2010) Migmatites formed by water-fluxed partial melting of a leucogranodiorite protolith: microstructures in the residual rocks and source of the fluid. *Lithos* 116:273–286
- Shimazaki H (1998) On the occurrence of silician magnetites. *Resour Geol* 48:23–29
- Tegner C, Cawthorn RG, Kruger FJ (2006) Cyclicality in the Main and Upper Zones of the Bushveld Complex, South Africa: crystallization from a zoned magma sheet. *J Petrol* 47:2257–2279
- Tollari N, Barnes S-J, Cox R, Nabil H (2008) Trace element concentrations in apatites from the Sept-Îles Intrusive Suite, Canada—implications for the genesis of nelsonites. *Chem Geol* 252:180–190
- Toplis M, Carroll M (1995) An experimental study of the influence of oxygen fugacity on Fe-Ti oxide stability, phase relations, and mineral—melt equilibria in ferro-basaltic systems. *J Petrol* 36:1137–1170
- Toplis MJ, Corgne A (2002) An experimental study of element partitioning between magnetite, clinopyroxene and iron-bearing silicate liquids with particular emphasis on vanadium. *Contrib Mineral Petrol* 144:22–37
- Van Baalen MR (1993) Titanium mobility in metamorphic systems: a review. *Chem Geol* 110:233–249
- Yang S, Wang Z, Gui Y, Li C, Cai J (2009) Heavy mineral compositions of the Changjiang (Yangtze River) sediments and their provenance-tracing implication. *J Asian Earth Sci* 35:56–65